

# Patronus: Bringing Transparency to Diffusion Models with Prototypes

Nina Weng, Aasa Feragen, Siavash Bigdeli  
 Technical University of Denmark  
 {ninwe, afhar, sarbi}@dtu.dk

## Abstract

Diffusion-based generative models, such as Denoising Diffusion Probabilistic Models (DDPMs), have achieved remarkable success in image generation, but their step-by-step denoising process remains opaque, leaving critical aspects of the generation mechanism unexplained. To address this, we introduce Patronus, an interpretable diffusion model inspired by ProtoPNet. Patronus integrates a prototypical network into DDPMs, enabling the extraction of prototypes and conditioning of the generation process on their prototype activation vector. This design enhances interpretability by showing the learned prototypes and how they influence the generation process. Additionally, the model supports downstream tasks like image manipulation, enabling more transparent and controlled modifications. Moreover, Patronus could reveal shortcut learning in the generation process by detecting unwanted correlations between learned prototypes. Notably, Patronus operates entirely without any annotations or text prompts. This work opens new avenues for understanding and controlling diffusion models through prototype-based interpretability. Our code is available at <https://github.com/nina-weng/patronus>.

## 1. Introduction

The generative capabilities of modern machine learning models, particularly diffusion models, have advanced significantly, enabling the creation of highly realistic samples that closely resemble real-world data. However, their opacity raises critical concerns, including bias amplification [22], unsafe content [27], and copyright violations [31]. Their lack of transparency makes it difficult to detect and mitigate these risks, highlighting a fundamental question: *How can the diffusion generation process be interpreted and understood?* Specifically, **what** visual patterns emerge during generation, **where** and **when** they appear, and to what extent they can be **controlled**. Addressing these questions is essential – not only for improving generative modeling but also for ensuring interpretability, transparency, and ethical deployment, aligning with regulatory frameworks

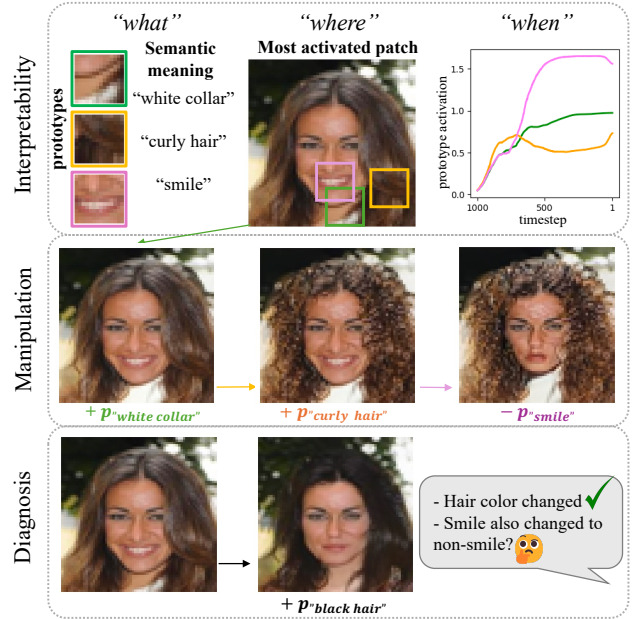


Figure 1. **Interpretability, manipulation, and diagnostic capabilities of Patronus.** Interpretability: By integrating a prototypical network as the encoder, *Patronus* learns semantic prototypes (“what”) and explains the generative process by revealing *where* and *when* they emerge. Manipulation: By adjusting the prototype activation vector, *Patronus* enables targeted semantic image editing. Diagnosis: Semantic image editing may reveal unwanted correlations learned from the training data during generation. Note that *Patronus* operates without any annotations or text prompts.

such as the EU AI Act.

Existing approaches to improving interpretability in diffusion-based visual generation typically fall into two categories. The first relies on post-hoc analysis to investigate how semantic information are encoded in intermediate representations [10, 16, 18, 25, 29, 30]. However, this method is inherently retrospective and limited in its ability to provide direct control over generation. The second approach introduces additional encoder-based semantic vectors for diffusion guidance [19, 26, 33], which improves controllability, but often resulting in representations that are diffi-

cult to interpret. Moreover, these methods tend to capture global (e.g. face shape, pose) rather than fine-grained patterns (e.g. hair details, facial expressions, make-up details), and the latter are crucial for interpretability.

To address these limitations, we aim to develop a method that fulfills two key objectives: (1) embedding interpretability directly into the model architecture, thereby providing **intrinsic transparency** and eliminating the need for post-hoc analysis of high-dimensional latent features; (2) moving interpretability a step further from global to **local semantic meanings** and enabling the controllability.

Drawing inspiration from ProtoPNet [4], a deep learning framework that enhances interpretability through prototypical networks, we propose *Patronus*, a novel diffusion-based generative model augmented with a prototypical network for semantic encoding. Our approach trains prototype features to capture localized patterns within image patches, and uses prototype activation vector to encode the presence of semantic information for diffusion guidance. This design effectively reduces the latent dimensionality while preserving sufficient semantic information. Furthermore, by manipulating the activation vector as conditioning signals, we enable direct visualization of the learned prototypes, enhancing interpretability and control.

**Our contributions are summarized as follows:**

1. We propose *Patronus*: An interpretable diffusion model for image generation which incorporates a prototypical network for prototype learning and representation, alongside a conditional guidance by a prototype activation vector—entirely without extra annotations.
2. We introduce a novel method for visualizing learned prototypes, revealing how each prototype influences the generation process, and enabling manipulation of the prototype activation vector for image generation.
3. Through extensive experiments, we show that *Patronus* effectively captures semantically meaningful features within images, and achieves competitive latent quality and generation quality compared to SOTA methods.
4. We demonstrate the potential of *Patronus* to diagnose unwanted correlations in datasets, offering a valuable tool for mitigating biases in generative models and promoting fairness in their deployment.

## 2. Related Work

### 2.1. Visual Prototype Explanations

Our work is closely related to and motivated by ProtoPNet [4] and its subsequent developments [5, 7, 24, 32], which build interpretable deep learning frameworks by learning *prototypes*, intermediate representations of visually similar patterns between training and inference images.

Under such a design, a key challenge is visualizing the

learned prototypes. Li et al. [20] used a decoder to reconstruct prototypes, while ProtoPNet replaced it by identifying the closest matching encoded representations from the training set via distance comparisons, with the improvement of flexible patch sizes. Follow-up works explore alternative prototype design but do not enhance visualization.

### 2.2. Interpretable Diffusion Models

Recent work on explaining diffusion models has focused on the following two directions: (1) **Semantic interpretation of the internal features**: Investigating how diffusion models encode and represent semantic information within their intermediate layers; and (2) **Construction of semantic vectors from an additional encoder for diffusion guidance**: Branching out another auto-encoder to construct a semantic vector for diffusion process guidance.

**Semantic Interpretation of Internal Features.** Diffusion models were traditionally viewed as lacking internal representations compared to other generative models, like VAE [14] and GAN [8]. However, Kwon et al. [16] pointed out that *diffusion models possess a semantic latent space* within the U-Net’s intermediate layer. They leverage the bottleneck for semantic control over the denoising process and propose the asymmetric reverse process to edit the image based on the discovered semantic meaning.

Building on this idea, researchers have sought to interpret the latent space (called *h-space* in [16]) of diffusion models by grouping the latent vectors with different noise schedules [18], applying pullback metrics to obtain meaningful local latent basis [25], and uncovering semantically meaningful directions by both PCA and linear properties of the semantic latent space [10]. Other works [29, 30] extract structural information from the latent space and use it for I2I translation or prompted generation tasks.

**Autoencoder-based semantic feature extraction for guidance.** An alternative way to enhance the interpretability of diffusion models is to integrate an additional encoder to extract semantic features for guidance. DiffAE [26] pioneered this idea using a learnable encoder for latent semantics. Expanding on this, DiffuseGAE [19] proposed a Group-supervised AutoEncoder module to achieve better latent disentanglement, while InfoDiffusion [33] reduced latent dimensionality and enforced mutual information constraints for more effective learning.

While these methods extract global semantic features, *Patronus* instead captures local features through a prototypical network. Another key distinction lies in how the diffusion model is guided: Rather than direct semantic information, we use the *prototype activation vector*. This approach significantly reduces the dimensionality needed for

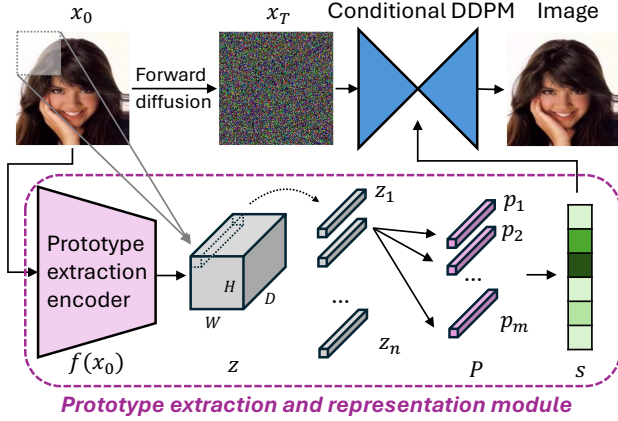


Figure 2. **Overview of Patronus**: contains a prototypical network for prototype extraction and a conditional DDPM for generation.

diffusion guidance while preserving enough capacity in prototype features to encode the same semantic information.

### 3. Method: Patronus Framework for Interpretable DDPM-based Image Generation

Our proposed model, **Patronus: Prototype-Assisted Transparent Diffusion Model**, is illustrated in Fig. 2. Designed to enhance transparency and interpretability in diffusion models, *Patronus* incorporates a prototype extraction and representation module (bottom part of Fig. 2). This module learns patch-based prototypes within the image and computes similarity score for each prototype, which are then used to condition the diffusion process (top part of Fig. 2). We elaborate on the details of the prototype extraction and representation module in Sec. 3.1 and the conditional DDPM in Sec. 3.2. Furthermore, we explain how transparency and interpretability are achieved, including sampling strategy and manipulations, in Sec. 3.3. We detail the unconditional sampling strategies in Sec. 3.4, and furthermore prove that adding conditions does not degrade the denoiser training in Sec. 3.5.

#### 3.1. Prototype Extraction and Representation

This module, inspired by ProtoPNet [4], consists of two key components: The **prototype encoder** transforms input images into patch-based feature representations. Utilizing the properties of convolutional neural networks (CNNs), each output neuron in the feature map corresponds to a specific patch of the input image, determined by the network’s receptive field. This patch-based representation enables the model to focus on localized patterns and learn fine-grained prototypes. The **activation vector** is derived by calculating similarity scores for each learned prototype, based on the distance between encoded patches and prototypes, where

higher scores indicate stronger matches.

This module works as follows: As shown in Fig. 2, given an input image  $x_0$ , the prototype encoder  $f$  extracts features  $z = f(x_0)$  into a tensor of shape  $H \times W \times D$ . The network learns  $m$  prototypes in the latent feature space during training, denoted as  $P = \{p_j\}_{j=1}^m$ , each with the shape  $1 \times 1 \times D$ <sup>1</sup>. Each prototype  $p_j$  can be interpreted as a latent encoding of a patch in the original pixel space. This patch, importantly, need not exist in the dataset but should lie within the plausible data distribution.

For the encoder output  $z = f(x_0)$ , each spatial region within  $z$  that corresponds to the same size as a prototype ( $1 \times 1 \times D$ ) can be interpreted as representing a patch of  $x_0$ . Thus,  $z$  can be decomposed into smaller regions as follows:  $z = \{z_i\}_{i=0}^n$ , where  $n$  denotes the total number of patches encoded in  $z$ . In our case,  $n = H \times W$ .

To calculate the similarity between the encoded features  $z$  and the learned prototypes  $P$ , we begin by computing the squared  $L_2$  distance between each spatial feature  $z_i$  and each prototype  $p_j$ :  $d^2(z_i, p_j) = \|z_i - p_j\|^2$ . Next, the minimum distance across the spatial dimensions is selected for each prototype, given by:  $d_{min,j}^2 = \max(-d_j^2, \text{kernel size})$ , where  $d_j^2$  is the set of distances for the  $j$ th prototype across all spatial positions, and the kernel size aligns with the feature map’s spatial dimensions  $H$  and  $W$ .

The sequence of minimum distances for all prototypes is converted into an activation vector  $s$  using a log transformation:  $s = \log(\frac{d^2+1}{\epsilon})$ , where  $\epsilon$  is a small positive constant.

#### 3.2. Conditional Diffusion Process

Denoising diffusion probabilistic models (DDPM) form a class of generative models that learn data distributions by iteratively denoising a noisy latent representation. The process involves (1) **a forward diffusion process**, where Gaussian noise is progressively added to a data sample  $x_0$  over  $T$  timesteps, producing noisy latents  $x_t$ , defined as

$$q(x_t | x_{t-1}) = \mathcal{N}(x_t; \sqrt{\alpha_t}x_{t-1}, (1 - \alpha_t)\mathbf{I}). \quad (1)$$

Here, the marginal distribution of  $x_t$  given  $x_0$  is:

$$q(x_t | x_0) = \mathcal{N}(x_t; \sqrt{\bar{\alpha}_t}x_0, (1 - \bar{\alpha}_t)\mathbf{I}), \quad (2)$$

where  $\bar{\alpha}_t = \prod_{i=1}^t \alpha_i$  and  $\alpha_t = 1 - \beta_t$ , where  $\beta_t$  is the variance of the Gaussian noise added at  $t$ . Furthermore, DDPMs rely on (2) **a reverse generative process** that removes noise given  $t$ :

$$p_\theta(x_{t-1} | x_t) = \mathcal{N}(x_{t-1}; \mu_\theta(x_t, t), \Sigma_\theta(x_t, t)) \quad (3)$$

To enable **conditional generation**, we modify the reverse process to be conditioned on the prototype activation vector  $s$ . Therefore the updated reverse process is:

$$p_\theta(x_{t-1} | x_t, s) = \mathcal{N}(x_{t-1}; \mu_\theta(x_t, t, s), \Sigma_\theta(x_t, t)) \quad (4)$$

<sup>1</sup>whose generalization to  $H_1 \times W_1 \times D$  as in [4] is straightforward.

The training objective remains based on the standard noise-prediction loss used in DDPM. For a given noisy sample  $x_t$ , timestep  $t$  and noise  $\epsilon$  the model minimizes the loss:

$$\mathcal{L}_{ddpm} = \mathbb{E}_{x_0, \theta, t} [\|\epsilon - \epsilon_\theta(x_t, t, s)\|^2], \quad (5)$$

where  $\epsilon_\theta$  is the learned denoiser. As the loss indicates, our guidance does not change the model’s output – it only encourages its reasoning to utilize prototypes for transparency.

### 3.3. Transparency and Interpretability of Patronus

The similarity score  $s_j$  quantifies the activation of the  $j_{th}$  prototype in a given input, indicating the presence of specific semantic patterns. The model thus conditionally generates samples guided by interpretable semantic information.

**Visualizing learned prototypes.** Integrating a prototypical network as a semantic meaning extraction module brings inherent interpretability: Each learned prototype vector  $p_j$  represents a patch in the image domain. In ProtoPNet [4], those patches are retrieved via a greedy search of the training set and finding the patch with closest embedding to  $p_j$ .

We argue that the learned prototypes do not need to correspond directly to specific training patches but should instead align with the overall distribution of the training data. To support this, we propose a novel prototype visualization method with the following steps:

1. Compute the activation vector  $s = \{s_j\}_{j=1}^m$ , for a given sample  $x_0$ , where  $s_j$  represents the similarity score between  $x_0$  and the  $j_{th}$  prototype.
2. For target prototype  $J$ , increase its similarity score  $s_J$  to the plausible maximum while keeping all other scores unchanged. The updated activation vector  $s' = \{s'_j\}_{j=1}^m$  is defined as:  $s'_j = \begin{cases} s_j, & \text{if } j \neq J \\ \max(s_X), & \text{if } j = J \end{cases}$ . Here,  $s_X$  represents similarity scores from a representative subset, constraining  $s_J$  within a plausible range.
3. Using the updated activation vector  $s'$  to sample a new image  $x'$  conditioned on  $s'$ .
4. Identify the most activated patch  $x'_i$  in  $x'$  that corresponds to the target prototype  $J$ . This patch  $x'_i$  serves as the visual representation of  $p_J$ .

Note that this method could also be used to visualize prototypes in other prototype based deep learning models.

### Manipulation using the prototype activation vector.

Manipulating images is a natural downstream task for *Patronus*, as adjusting a specific prototype similarity score  $s_j$  and conditionally generating a new sample allows us to effectively and semantically control the image content:

$$p_\theta(x_{t-1} | x_t, s') = \mathcal{N}(x_{t-1}; \mu_\theta(x_t, t, s'), \Sigma_\theta(x_t, t)) \quad (6)$$

### Deterministic reverse process via DDIM sampling.

Both the visualization of prototypes and their manipulation via activation vectors build on the DDPM sampling process. However, for stricter control over the stochasticity introduced by random noise, the Denoising Diffusion Implicit Models (DDIM) sampler provides an alternative approach:

$$p_\theta(x_{t-1} | x_t, s) = \mathcal{N}(x_{t-1}; \mu_t, \sigma^2 \mathbf{I}) \quad (7)$$

$$\mu_t = \sqrt{\bar{\alpha}_{t-1}} \cdot \hat{x}_0 + \sqrt{1 - \bar{\alpha}_{t-1} - \sigma^2} \cdot \epsilon_\theta(x_t, t, s) \quad (8)$$

$$\sigma^2 = \eta^2 \cdot \frac{1 - \bar{\alpha}_{t-1}}{1 - \bar{\alpha}_t} \cdot (1 - \frac{\bar{\alpha}_t}{\bar{\alpha}_{t-1}}) \quad (9)$$

By setting  $\eta = 0.0$ , the process becomes deterministic, leading to the following update for the reverse process:

$$x_{t-1} = \sqrt{\bar{\alpha}_{t-1}} \cdot \hat{x}_0 + \sqrt{1 - \bar{\alpha}_{t-1}} \cdot \epsilon_\theta(x_t, t, s), \quad (10)$$

where  $\hat{x}_0$  is the estimated denoised image, computed as:

$$\hat{x}_0 = \frac{1}{\sqrt{\bar{\alpha}_t}} (x_t - \sqrt{1 - \bar{\alpha}_t} \cdot \epsilon_\theta(x_t, t, s)). \quad (11)$$

This DDIM sampling requires  $x_T$ , which represents the initial noise in the diffusion process. This could be obtained by performing a deterministic backward generative process:

$$x_{t+1} = \sqrt{\bar{\alpha}_{t+1}} \cdot \hat{x}_0 + \sqrt{1 - \bar{\alpha}_{t+1}} \cdot \epsilon_\theta(x_t, t, s) \quad (12)$$

### 3.4. Unconditional Sampling Strategy

For unconditional sampling, we adopt the approach of [26], training an auxiliary latent diffusion model  $p(s_{t-1} | s_t, t)$  to sample  $s$ . During training, we first jointly optimize the prototypical encoder with the conditional DDPM; subsequently, the latent diffusion model is trained while keeping the previously learned parameters fixed.

### 3.5. Adding the Condition to the Objective

In *Patronus*, the prototype encoder is jointly optimized with the denoiser. To show that this simultaneous training does not degrade the generated distribution, we analyze how updating the condition  $s$  affects the likelihood. For ease of derivation, we use the Evidence Lower Bound (ELBO) as an equivalent objective to generalize denoising losses [11].

**Proposition.** *Optimizing the conditioning variable  $s$  with denoising loss cannot degrade the quality of the results.*

*Proof.* Assume that  $s^i$  is updated to  $s^{i+1}$  via a gradient step optimizing the ELBO. By definition of gradient descent:

$$\text{ELBO}(s^i) \leq \text{ELBO}(s^{i+1})$$

The ELBO loss is given by:

$$\text{ELBO}(s^i) = \mathbb{E} [\log p(x_0, x_{1:T} | s^i) - \log q(x_{1:T} | x_0)]$$



Since the ELBO is a variational lower bound on the marginal log-likelihood  $\log p(x_0)$ , an increase in ELBO generally implies that the approximate posterior distribution  $q(x_{1:T}|x_0)$  better captures the true posterior. However, increasing ELBO does not necessarily increase the likelihood  $p(x_0|s)$  itself. We therefore consider two possible cases:

**Case 1:** If  $p(x_0|s^i) \leq p(x_0|s^{i+1})$ , then the update improves the likelihood of  $x_0$  under the model, directly enhancing the sample quality, as higher likelihood generally corresponds to more accurate or better-calibrated samples. Here, optimization has both increased the ELBO and improved the likelihood.

**Case 2:** If instead, we have  $p(x_0|s^i) > p(x_0|s^{i+1}) > p(x_0)$ , then the likelihood has not increased, but it remains greater than the marginal likelihood  $p(x_0)$ . In this case, we analyze the difference between likelihood and ELBO:

$$p(x_0|s^i) - \text{ELBO}(s^i) > p(x_0|s^{i+1}) - \text{ELBO}(s^{i+1}).$$

As the gap between likelihood and ELBO shrinks, ELBO becomes a tighter approximation to the true marginal log-likelihood  $\log p(x_0)$ . Thus, while the likelihood itself may not have increased, our approximation is now more reliable.

In both cases, optimizing  $s$  has positive impact and cannot degrade the quality of the results: Improved likelihood and better sample quality (Case 1), or a tighter ELBO bound, refining likelihood approximation (Case 2).  $\square$

This analysis is not applicable where a different objective is used to train the latent condition (e.g. InfoDiffusion [33]).

## 4. Experiments and Results

In our experiments, we first assess the semantic meaning of learned prototypes (Sec. 4.1), by evaluating their ability to capture and reconstruct meaningful visual patterns through interpolation, extrapolation (prototype visualization), and manipulation tasks. We then analyze prototype quality and generation performance (Sec. 4.2, 4.3). Finally, we explore how *Patronus* aids in diagnosing diffusion models by identifying potentially unwanted correlations via prototype similarity scores (Sec. 4.4).

We use five datasets: Quantitative evaluation on FMNIST [36], Cifar10 [15], FFHQ [13]; qualitative analysis on CheXpert [12]; and in-depth quantitative and qualitative experiments on CelebA [21]. We use 100 prototypes for all datasets except FMNIST, which has 30. Prototypes are encoded with a shape of (1,1,128). See Appendix for details.

### 4.1. Semantic Meaning of the Learned Prototypes.

**Capturing high level semantic features.** To check that the learned prototypes are semantically meaningful, we ex-

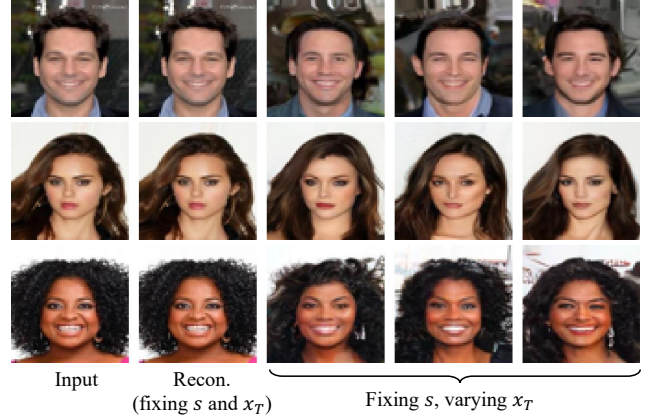


Figure 3. Reconstruction and variations with fixed  $s$ , random  $x_T$ .

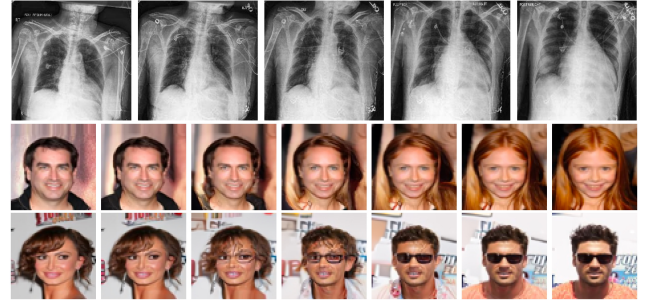


Figure 4. **Interpolation between two images.** First row: CheXpert [12], from 75-year-old female *w/o* enlarged heart (left) to 27-year-old male *w/* enlarged heart (right). Last two rows: CelebA.

tract the prototype activation vector  $s = \text{Enc}(x_0)$  and sample random noise  $x_T \sim \mathcal{N}(0, \mathbf{I})$  to generate new images  $\hat{x}(s, x_T)$ . Fig. 3 presents one reconstructed image (using the same  $x_T$ ) with three variations (using random  $x_T$ ). The results show that the majority of semantic information in the images is accurately recreated, confirming that the prototypes effectively capture meaningful semantic features.

**Interpolation.** Given two images  $x_0^1$  and  $x_0^2$ , we first retrieve its corresponding prototype activation vector and starting noise by reverse DDIM process:  $(s^1, x_T^1)$  and  $(s^2, x_T^2)$ , and then generate new samples using  $(\text{Lerp}(s^1, s^2; t), \text{Slerp}(x_T^1, x_T^2; t))$  for steps  $t \in [0, 1]$ , where Lerp/Slerp represents linear/spherical linear interpolation respectively. Results are shown in Fig. 4.

**Visualization of the learned prototypes.** A key distinction of our proposed method compared to other autoencoder-based diffusion models lies in the intrinsic interpretable semantic latent through visualization. Ideally, by training, each prototype inherently represents distinct content, and our approach is explicitly designed to allow

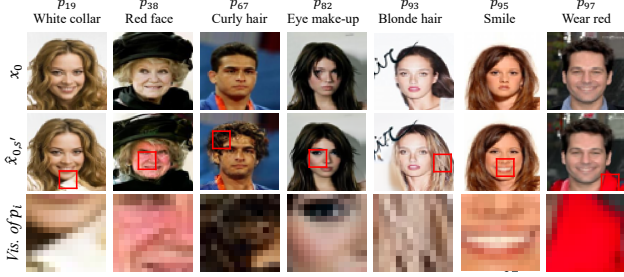


Figure 5. **Visualization of selected prototypes and their semantic interpretations.** Here,  $x_0$  denotes the original image,  $\hat{x}_{0,s'}$  denotes the generated image guided by condition  $s'$ , where  $s'$  is the enhanced prototype activation vector on  $j$ -th prototype. Red rectangle highlights the most activated patch in  $\hat{x}_{0,s'}$ , which is considered as the visual representation of the chosen prototype, also shown in the third row. Note that prototype semantics are not pre-annotated but inferred through observation.



Figure 6. **Consistency of prototype visualization.** We randomly select four samples and generate their enhanced images conditioned on prototype  $j$ . The most activated patch, representing the chosen prototype, remains consistent across all samples.

visual interpretation of these representations. In practice, we maximize the similarity score of selected prototype and identify the image patch where each prototype responds most strongly – a process we refer to as extrapolation, in contrast to interpolation. Detailed steps are provided in Sec. 3.3. In Fig. 5 we visualize selected prototypes and listed their semantic meanings from observation on the top.

**Consistency of prototype visualization.** Fig. 6 shows prototype visualization across four random samples for a fixed prototype. The most activated patches, representing the learned prototypes, remain consistent across samples.

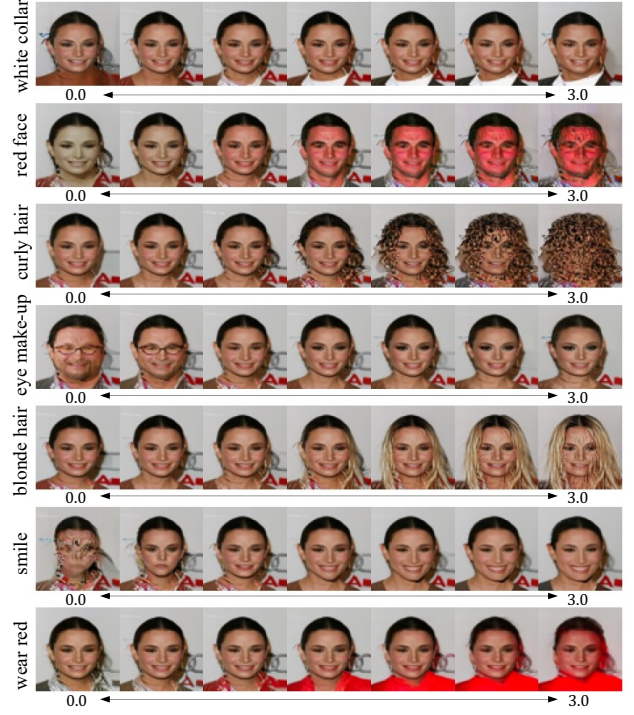


Figure 7. **Extrapolation** of prototype magnitude between 0 to 3.

**Manipulation and extrapolation.** By adjusting the condition  $s$  we can edit the image with specific semantic requests. As shown in Fig. 1, we enhance features like “white collar” and “curly hair” and diminish “smile” by modifying the corresponding prototype similarity scores. Furthermore, pushing a selected dimension of  $s$  to extreme values (ranging from 0.0 to 3.0) results in a smooth and continuous enhancement of the associated semantic information, as demonstrated in Fig. 7. Unlike interpolation, which remains within the observed range, this process extends beyond the original data distribution, making it an *extrapolation*.

## 4.2. Prototype Quality

**Prototype capability in semantic representation.** Following [33], we test the prototype quality via a downstream classification task on the prototype activation vectors  $s$  using a logistic regression classifier trained with 5-fold cross validation, reporting AUROC in Tab. 1 & 2. Our model outperform 3 out of 4 datasets in latent (prototype) quality, with particularly strong performance on CelebA and FFHQ. The lower latent quality for FMNIST may stem from *Patronus* prioritizing localized features, while DiffAE and InfoDiff emphasize global structures, which better capture the semantic information of FMNIST due to its high inter-class variability. For the datasets where semantic information is more localized, *Patronus* achieves a marked improvement.



Table 1. **Prototype quality and generation quality on CelebA.**

	TAD $\uparrow$	Attrs $\uparrow$	Latent AUROC $\uparrow$	FID $\downarrow$
DiffAE [26]	0.16 $\pm$ 0.01	2.0 $\pm$ 0.0	0.80 $\pm$ 0.00	22.7 $\pm$ 2.1
InfoDiff [33]	0.30 $\pm$ 0.01	3.0 $\pm$ 0.0	0.84 $\pm$ 0.00	23.6 $\pm$ 1.3
<i>w/</i> learned <i>z</i>	0.30 $\pm$ 0.01	3.0 $\pm$ 0.0	0.84 $\pm$ 0.00	22.3 $\pm$ 1.2
Patronus	<b>0.43<math>\pm</math>0.02</b>	<b>9.0<math>\pm</math>0.0</b>	<b>0.87<math>\pm</math>0.00</b>	14.6 $\pm$ 0.1
<i>w/</i> learned <i>s</i>	<b>0.43<math>\pm</math>0.02</b>	<b>9.0<math>\pm</math>0.0</b>	<b>0.87<math>\pm</math>0.00</b>	<b>4.8<math>\pm</math>0.0</b>

Table 2. **Prototype quality and generation quality on Fashion-MNIST, Cifar-10, and FFHQ.**

	FMNIST		Cifar10		FFHQ	
	Latent AUROC $\uparrow$	FID $\downarrow$	Latent AUROC $\uparrow$	FID $\downarrow$	Latent AUROC $\uparrow$	FID $\downarrow$
DiffAE [26]	0.84 $\pm$ 0.00	8.2 $\pm$ 0.3	0.40 $\pm$ 0.01	32.1 $\pm$ 1.1	0.61 $\pm$ 0.00	31.6 $\pm$ 1.2
InfoDiff [33]	<b>0.84<math>\pm</math>0.00</b>	8.5 $\pm$ 0.3	0.41 $\pm$ 0.00	32.7 $\pm$ 1.2	0.61 $\pm$ 0.00	31.2 $\pm$ 1.6
<i>w/</i> learned <i>z</i>	<b>0.84<math>\pm</math>0.00</b>	7.4 $\pm$ 0.2	0.41 $\pm$ 0.00	31.5 $\pm$ 1.8	0.61 $\pm$ 0.00	30.9 $\pm$ 2.5
Patronus	0.82 $\pm$ 0.00	14.7 $\pm$ 0.3	<b>0.54<math>\pm</math>0.01</b>	32.9 $\pm$ 0.4	<b>0.92<math>\pm</math>0.00</b>	37.3 $\pm$ 0.2
<i>w/</i> learned <i>s</i>	0.82 $\pm$ 0.00	<b>2.6<math>\pm</math>0.1</b>	<b>0.54<math>\pm</math>0.01</b>	<b>8.0<math>\pm</math>0.1</b>	<b>0.92<math>\pm</math>0.00</b>	<b>24.1<math>\pm</math>0.1</b>

**Prototype disentanglement.** We quantify the disentanglement on CelebA using TAD [37]. Following [33], we first remove the highly correlated attributes, then compute the AUROC score for each dimension of the prototype activation vector *s*. An attribute is “captured” if any dimension achieves AUROC  $> 0.75$ . TAD is the sum of AUROC differences between the top two predictive dimensions per captured attribute. As shown in Tab. 1, *Patronus* outperforms previous models in both TAD and captured attributes.

### 4.3. Generation Quality

We assess generative quality using the Fréchet Inception Distance (FID), averaged over five random test sets of 10,000 images. Evaluation covers both unconditional and prototype-conditioned generation, where the latter incorporates learned prototype activation vectors from the test set (see Tab. 1 & 2). *Patronus* significantly outperforms previous methods in prototype-conditioned generation across all four datasets. In the unconditional setting, it achieves state-of-the-art performance on CelebA and remains competitive on others; noting that its effectiveness depends on the training quality of both *Patronus* and the latent diffusion model.

### 4.4. Diagnosing Generative Models with Prototypes

We manipulated a subset of CelebA to introduce an unwanted correlation between hair color and smile: all blonde/brown-haired images smile, while black-haired ones do not. Fig. 8 visualizes the prototype for “smile” alongside one for each hair color categories. The parentheses list the Spearman correlation with the “smile” prototype, and the AUROC score for predicting the hair color using this prototype similarity score alone. Results confirm the model captures the introduced bias, as smile positively correlates with blonde/brown hair but not black. Prototypes for “smile” and hair colors were chosen based on the highest AUROC for

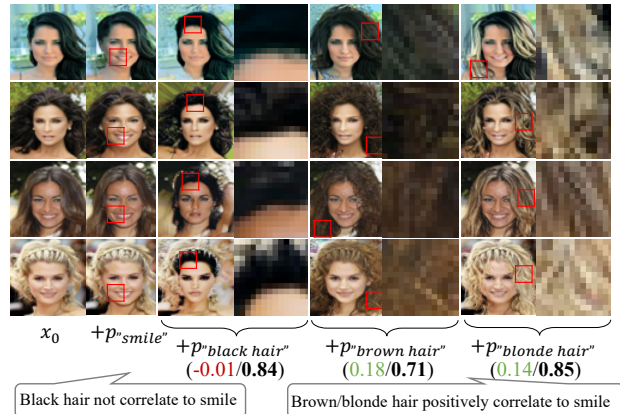


Figure 8. *Patronus* captures unwanted correlations of attributes (bias). We present four samples with their generated outputs, enhanced on a smile-related prototype and three hair-color prototypes. Prototypes are selected based on observation, with correctness confirmed by choosing the highest AUROC (bold value after “/”) for single-dimension prediction. The Spearman correlation between hair-color and smile prototypes, shown in green (positive) and red (negative), highlights dataset bias. It is interesting to see that enhancing the black hair prototype shifts generated images from smiling to non-smiling, and vice versa. Noted that the reported values are computed on the entire test set.

single-dimension *s* prediction.

Interestingly, enhancing a single prototype reveals unwanted correlations in the generated images. For example, increasing the black hair prototype shifts the smile property from “smile” to “non-smile” and vice versa (see Fig. 8). Similar patterns emerge without subset manipulation. In Fig. 7, increasing “white collar” enhances male features, while decreasing “eye makeup” reduces female features.

This emphasizes how *Patronus* can be utilized to discover unwanted model behavior.

## 5. Discussion and Conclusion

**Prototypes Emerge at Different Times during Generation.** Given a generated image, *Patronus* reveals when each prototype emerges in the generation process by obtaining the prototype similarity score from estimated  $\hat{x}_0$  at each timestep (more details in Appendix), as shown in the top-right corner of Fig. 1. Thus, by subtracting the two time-sequential *s* of the semantically-enhanced image  $\hat{x}_{0,s_t}$  and  $x_0$ , we illustrate how each prototype emerges temporally in the diffusion process. As shown in Fig. 9, none of the prototypes have a significant emergence in the first 200 stages of generation. Interestingly, prototypes relating to lower spatial frequency attributes appear earlier during generation, such as “wearing red”; while higher spatial frequency attributes, like “curly hair”, emerge later in the generation process.

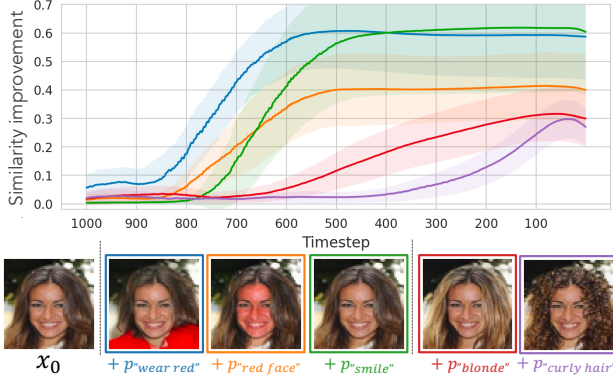
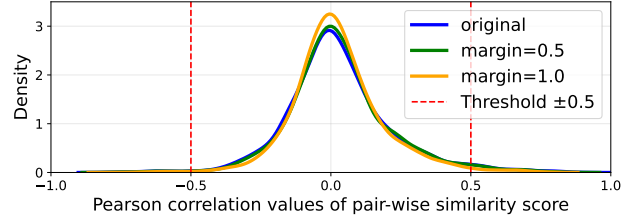


Figure 9. **Different prototypes emerge at different stages of the diffusion process.** The similarity score improvement between an edited image targeting prototype  $j$  and the original image reflects how  $p_j$  emerges over time. Here we show the average and standard deviation (as shadow) of similarity score improvement from 100 randomly generated samples. See text for a discussion on results.

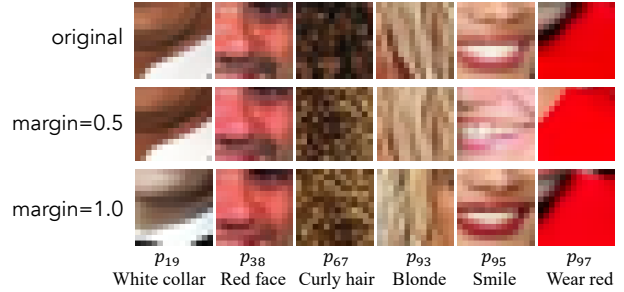
**Prototype Correlation and Collapse.** We test whether correlation between prototypes is caused by *prototype collapse*, where multiple prototypes represent the same semantics. To assess this, we introduce a Prototype Distinct Loss to encourage prototype disentanglement and evaluate its impact compared to using the denoiser loss alone. The Prototype Distinct Loss is defined as:  $\mathcal{L}_{distinct} = \frac{1}{N} \sum_{i=1}^N \max(0, \delta - \min_{j \neq i} D_{ij})$ , where  $D$  is the cosine distance with absolute similarity:  $D_{ij} = 1 - \left| \frac{p_i \cdot p_j}{\|p_i\| \|p_j\|} \right|$ . The margin  $\delta$  is set to 0.5 and 1.0. Notably, setting  $\delta = 1.0$  enforces prototypes to be orthogonal. We initialize the new model using the original network parameters and train it for an additional 100 epochs using  $L_{ddpm} + L_{distinct}$ . Fig. 10 shows that the new models do not see a substantial change in the learned prototypes, suggesting that the prototypes optimized via the denoising objective are already sufficiently decorrelated without explicit regularization.

**Limitations of Cross-Modal Interpretability.** We emphasize interpreting diffusion models *without* cross-modality by design for two key reasons:

- Language’s limitation in representing complexity: While language, as a discursive symbolism, serves as a powerful medium for interpretation, it alone cannot fully represent non-symbolic sensory and semantics complexity [17]. This is evident in the superior performance of multi-modal learning over single-modality; prior work [6, 9] further shows the restricted perceptual capacity of language-only generation by introducing visual cues.
- Inherited bias from the text embedding: (1) Incomplete text representations: if certain concepts are not explicitly named (e.g., medical devices in radiology reports), the model cannot learn their visual counterparts. (2) Spu-



(a) **Distribution of Pearson correlation values for prototype similarity scores**, computed from 1,024 randomly selected training samples. Results compare the original training and training with an additional loss term. The difference is minimal, with only a small fraction of pairs exceeding an absolute correlation of 0.5 (red dashed lines) for all cases.



(b) Prototype visualizations and their semantic interpretations remain consistent regardless of the additional loss.

Figure 10. **Effect of additional loss on prototype diversity.** (Top) Pearson correlation distribution of prototype similarity scores shows minimal differences regardless of additional loss. (Bottom) Prototype visualizations remain consistent, indicating negligible impact on semantic representations.

rious correlations: text data may encode unintended biases, such as differing report detail levels by patient demographics, which may propagate into generated images.

**Do We Capture All Relevant Attributes?** While *Patronus* shows great ability in capturing attributes, we notice that global features, e.g. gender and age, are harder to find in one specific prototype. This could result from the patch-based prototypical encoder, making non-local features hard to capture. See Appendix for illustrative visual examples.

## 5.1. Conclusion

We propose *Patronus*, an interpretable diffusion model integrated with a prototypical network. It enables intuitive interpretation of the generation process by visualizing learned prototypes (*what*) and identifying *where* and *when* they appear. It also supports semantic manipulation through prototype activation vector. Experiments show that *Patronus* achieves competitive performance and learns meaningful prototype-based representations. We further explore its capability to diagnose unwanted correlations in the generative process. We believe *Patronus* offers valuable insights



into interpretable diffusion models by bridging diffusion and prototypical networks.

## Acknowledgements.

Work on this project was partially funded by DTU Compute, the Technical University of Denmark; the Pioneer Centre for AI (DNRF grant nr P1); and the Novo Nordisk Foundation through the Center for Basic Machine Learning Research in Life Science (MLLS, grant NNF20OC0062606). The funding agencies had no influence on the writing of the manuscript nor on the decision to submit it for publication.

## References

- [1] François Bellemare, Alphonse Jeanneret, and Jacques Cou-  
ture. Sex differences in thoracic dimensions and configu-  
ration. *American journal of respiratory and critical care  
medicine*, 168(3):305–312, 2003. 20
- [2] Jean-François Bellemare, Marie-Pierre Cordeau, Pierre  
Leblanc, and François Bellemare. Thoracic dimensions at  
maximum lung inflation in normal subjects and in patients  
with obstructive and restrictive lung diseases. *Chest*, 119(2):  
376–386, 2001. 20
- [3] Keno K Bressem, Lisa C Adams, Christoph Erxleben, Bernd  
Hamm, Stefan M Niehues, and Janis L Vahldiek. Compar-  
ing different deep learning architectures for classification of  
chest radiographs. *Scientific reports*, 10(1):13590, 2020. 15,  
17
- [4] Chaofan Chen, Oscar Li, Daniel Tao, Alina Barnett, Cynthia  
Rudin, and Jonathan K Su. This looks like that: deep learn-  
ing for interpretable image recognition. *Advances in neural  
information processing systems*, 32, 2019. 2, 3, 4
- [5] Jon Donnelly, Alina Jade Barnett, and Chaofan Chen. De-  
formable protopnet: An interpretable image classifier using  
deformable prototypes. In *Proceedings of the IEEE/CVF  
conference on computer vision and pattern recognition*,  
pages 10265–10275, 2022. 2
- [6] Rinon Gal, Yuval Alaluf, Yuval Atzmon, Or Patash-  
nik, Amit H Bermano, Gal Chechik, and Daniel Cohen-  
Or. An image is worth one word: Personalizing text-to-  
image generation using textual inversion. *arXiv preprint  
arXiv:2208.01618*, 2022. 8
- [7] Gaurav R Ghosal and Reza Abbasi-Asl. Multi-modal proto-  
type learning for interpretable multivariable time series clas-  
sification. *arXiv preprint arXiv:2106.09636*, 2021. 2
- [8] Ian Goodfellow, Jean Pouget-Abadie, Mehdi Mirza, Bing  
Xu, David Warde-Farley, Sherjil Ozair, Aaron Courville, and  
Yoshua Bengio. Generative adversarial nets. *Advances in  
neural information processing systems*, 27, 2014. 2
- [9] Yash Goyal, Tejas Khot, Douglas Summers-Stay, Dhruv Ba-  
tra, and Devi Parikh. Making the v in vqa matter: Elevating  
the role of image understanding in visual question answer-  
ing. In *Proceedings of the IEEE conference on computer  
vision and pattern recognition*, pages 6904–6913, 2017. 8
- [10] René Haas, Inbar Huberman-Spiegelglas, Rotem Mula-  
yoff, Stella Graßhof, Sami S Brandt, and Tomer Michaeli. Dis-  
covering interpretable directions in the semantic latent space  
of diffusion models. In *2024 IEEE 18th International Con-  
ference on Automatic Face and Gesture Recognition (FG)*,  
pages 1–9. IEEE, 2024. 1, 2
- [11] Jonathan Ho, Ajay Jain, and Pieter Abbeel. Denoising dif-  
fusion probabilistic models. *Advances in neural information  
processing systems*, 33:6840–6851, 2020. 4
- [12] Jeremy Irvin, Pranav Rajpurkar, Michael Ko, Yifan Yu, Sil-  
viana Ciurea-Ilcus, Chris Chute, Henrik Marklund, Behzad  
Haghighi, Robyn Ball, Katie Shpanskaya, et al. Chexpert:  
A large chest radiograph dataset with uncertainty labels and  
expert comparison. In *Proceedings of the AAAI conference  
on artificial intelligence*, pages 590–597, 2019. 5, 12
- [13] Tero Karras. A style-based generator architecture for genera-  
tive adversarial networks. *arXiv preprint arXiv:1812.04948*,  
2019. 5
- [14] Diederik P Kingma. Auto-encoding variational bayes. *arXiv  
preprint arXiv:1312.6114*, 2013. 2
- [15] Alex Krizhevsky, Geoffrey Hinton, et al. Learning multiple  
layers of features from tiny images. 2009. 5
- [16] Mingi Kwon, Jaeseok Jeong, and Youngjung Uh. Diffusion  
models already have a semantic latent space. *arXiv preprint  
arXiv:2210.10960*, 2022. 1, 2
- [17] Susanne K Langer. *Philosophy in a new key: A study in the  
symbolism of reason, rite, and art*. Harvard University Press,  
2009. 8
- [18] Sangyun Lee, Gayoung Lee, Hyunsu Kim, Junho Kim, and  
Youngjung Uh. Diffusion models with grouped latents for  
interpretable latent space. In *ICML 2023 Workshop on Struc-  
tured Probabilistic Inference {\&} Generative Modeling*,  
2023. 1, 2
- [19] Yipeng Leng, Qiangjuan Huang, Zhiyuan Wang, Yangyang  
Liu, and Haoyu Zhang. Diffusegae: controllable and high-  
fidelity image manipulation from disentangled representa-  
tion. In *Proceedings of the 5th ACM International Confer-  
ence on Multimedia in Asia*, pages 1–7, 2023. 1, 2
- [20] Oscar Li, Hao Liu, Chaofan Chen, and Cynthia Rudin. Deep  
learning for case-based reasoning through prototypes: A  
neural network that explains its predictions. In *Proceedings  
of the AAAI Conference on Artificial Intelligence*, 2018. 2
- [21] Ziwei Liu, Ping Luo, Xiaogang Wang, and Xiaoou Tang.  
Deep learning face attributes in the wild. In *Proceedings of  
International Conference on Computer Vision (ICCV)*, 2015.  
5
- [22] Sasha Luccioni, Christopher Akiki, Margaret Mitchell, and  
Yacine Jernite. Stable bias: Evaluating societal representa-  
tions in diffusion models. *Advances in Neural Information  
Processing Systems*, 36:56338–56351, 2023. 1
- [23] William F McCormick and JH Stewart. Age related changes  
in the human plastron: a roentgenographic and morphologic  
study. *Journal of Forensic Sciences*, 33(1):100–120, 1988.  
20
- [24] Yao Ming, Panpan Xu, Huamin Qu, and Liu Ren. Inter-  
pretable and steerable sequence learning via prototypes. In

- Proceedings of the 25th ACM SIGKDD International Conference on Knowledge Discovery & Data Mining*, pages 903–913, 2019. 2
- [25] Yong-Hyun Park, Mingi Kwon, Jaewoong Choi, Junghyo Jo, and Youngjung Uh. Understanding the latent space of diffusion models through the lens of riemannian geometry. *Advances in Neural Information Processing Systems*, 36: 24129–24142, 2023. 1, 2
- [26] Konpat Preechakul, Nattanat Chatthee, Suttisak Wizatwongsa, and Supasorn Suwajanakorn. Diffusion autoencoders: Toward a meaningful and decodable representation. In *Proceedings of the IEEE/CVF conference on computer vision and pattern recognition*, pages 10619–10629, 2022. 1, 2, 4, 7
- [27] Yiting Qu, Xinyue Shen, Xinlei He, Michael Backes, Savvas Zannettou, and Yang Zhang. Unsafe diffusion: On the generation of unsafe images and hateful memes from text-to-image models. In *Proceedings of the 2023 ACM SIGSAC conference on computer and communications security*, pages 3403–3417, 2023. 1
- [28] Radiology Masterclass. Chest x-ray appearances and patient age, n.d. Accessed: 2025-03-24. 20
- [29] Chenyang Si, Ziqi Huang, Yuming Jiang, and Ziwei Liu. Freeu: Free lunch in diffusion u-net. In *Proceedings of the IEEE/CVF Conference on Computer Vision and Pattern Recognition*, pages 4733–4743, 2024. 1, 2
- [30] Narek Tumanyan, Michal Geyer, Shai Bagon, and Tali Dekel. Plug-and-play diffusion features for text-driven image-to-image translation. In *Proceedings of the IEEE/CVF Conference on Computer Vision and Pattern Recognition*, pages 1921–1930, 2023. 1, 2
- [31] Nikhil Vyas, Sham M Kakade, and Boaz Barak. On provable copyright protection for generative models. In *International conference on machine learning*, pages 35277–35299. PMLR, 2023. 1
- [32] Chong Wang, Yuyuan Liu, Yuanhong Chen, Fengbei Liu, Yu Tian, Davis McCarthy, Helen Frazer, and Gustavo Carneiro. Learning support and trivial prototypes for interpretable image classification. In *Proceedings of the IEEE/CVF International Conference on Computer Vision*, pages 2062–2072, 2023. 2
- [33] Yingheng Wang, Yair Schiff, Aaron Gokaslan, Weishen Pan, Fei Wang, Christopher De Sa, and Volodymyr Kuleshov. Infodiffusion: Representation learning using information maximizing diffusion models. In *International Conference on Machine Learning*, pages 36336–36354. PMLR, 2023. 1, 2, 5, 6, 7
- [34] Nina Weng, Siavash Bigdeli, Eike Petersen, and Aasa Feragen. Are sex-based physiological differences the cause of gender bias for chest x-ray diagnosis? In *Workshop on Clinical Image-Based Procedures*, pages 142–152. Springer, 2023. 12
- [35] Nina Weng, Paraskevas Pegios, Eike Petersen, Aasa Feragen, and Siavash Bigdeli. Fast diffusion-based counterfactuals for shortcut removal and generation. In *European Conference on Computer Vision*, pages 338–357. Springer, 2024. 15, 17
- [36] Han Xiao, Kashif Rasul, and Roland Vollgraf. Fashion-mnist: a novel image dataset for benchmarking machine learning algorithms. *arXiv preprint arXiv:1708.07747*, 2017. 5
- [37] Eric Yeats, Frank Liu, David Womble, and Hai Li. Nashae: Disentangling representations through adversarial covariance minimization. In *European Conference on Computer Vision*, pages 36–51. Springer, 2022. 7

## Appendix

### A. Additional details of implementing *Patronus*

#### A.1. Interpretability: Locating Most Activated Patch for each Prototype

Given an input image  $x_0$  and a chosen prototype  $J$ , the most activated patch is determined as follows:

1. Compute the similarity score between each latent feature  $z_i$ , where  $i \in \{1, 2, \dots, N\}$ , and the prototype  $p_J$ . Identify the closest  $z_i$  as:

$$i' = \arg \min_i D(z_i, p_J)$$

where  $D(\cdot, \cdot)$  represents the chosen distance metric; in our case, it's the log transformed square  $L2$  distance (Sec. 3.1).

2. Map the index  $i'$  back to the spatial coordinates of the feature map. Using the receptive field of the encoder, locate the corresponding patch in the original image, as shown in Fig. 11.

#### A.2. Interpretability: Analyzing Prototype Emerge Time

**Retrieve prototype activation vector along generation process for one image.** For a given guidance  $s$  and starting noise  $x_T$ , we can sample a generated image  $x_0$ , where  $x_t$  denotes the intermediate state at each timestep. At each timestep  $t$ , the estimated denoised image  $\hat{x}_0^t$  is computed as:

$$\hat{x}_0^t = \frac{1}{\sqrt{\alpha_t}}(x_t - \sqrt{1 - \alpha_t} \cdot \epsilon_\theta(x_t, t, s)). \quad (13)$$

Here, the superscript  $t$  indicates that this estimate originates from timestep  $t$ . The prototype activation vector at timestep  $t$  is then obtained as:  $s^t = \text{Enc}(\hat{x}_0^t)$ . By repeating this process across all timesteps  $t$ , we obtain the sequence  $\{s^t\}_{t=0}^T$ . Extracting the  $j$ -th index from each activation vector yields  $\{s_j^t\}_{t=0}^T$ , which tracks how the  $j$ -th prototype is activated throughout the generation process for sample  $x_0$ .

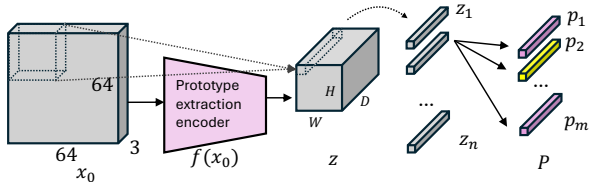


Figure 11. **Illustration on how to find the most activated patch given  $x_0$  regarding prototype  $J$ .** Here the shape of  $x_0$  ( $64 \times 64 \times 3$ ) serves as an example and should be generalizable to other scenarios.

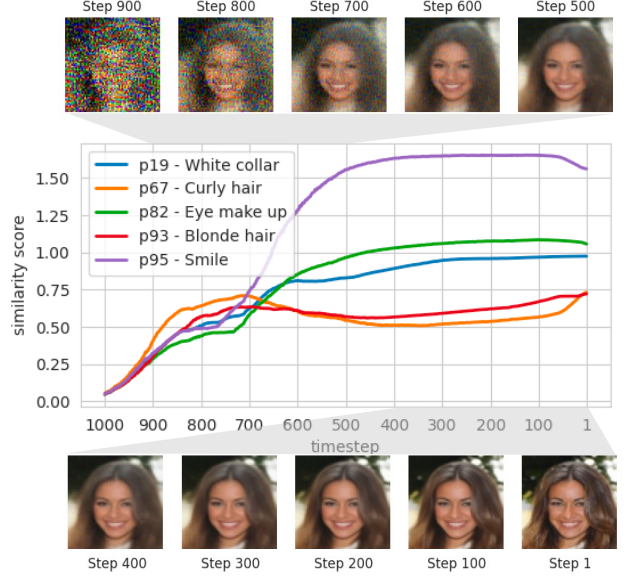


Figure 12. **Prototype emergence in a representative sample.** Generation dynamics for five selected prototypes.

**Examples of how prototypes emerge differently over time during diffusion.** Building on the illustrative example in Fig. 1, where specific semantic features are enhanced or suppressed using prototype activation vectors, we examine how the five selected prototypes emerge over time during the generation process. This is shown for the original image (Fig. 12), with the enhancement of the prototype “White collar” (Fig. 13), and with the enhancement of the prototype “Curly hair” (Fig. 14). Interestingly, when the “White collar” prototype is enhanced, its similarity score increases notably around timestep 700/1000 (Fig. 13). In contrast, when enhancing the “Curly hair” prototype, its similarity score begins to rise around timestep 200/1000 (Fig. 14). Note that larger  $t$  corresponds to an earlier stage of the diffusion process, which means “Curly hair” as a semantic information emerged later in diffusion generation process, compared to “White collar”.

This observation is further confirmed by the estimated denoised  $\hat{x}_0^t$  in Fig. 13 and Fig. 14. White clothing appears at an early stage of the denoised images, whereas although the hair becomes fluffier, the fine-grained curly texture only emerges around timestep 200 (bottom of Fig. 14). This difference is summarized in Fig. 15, where we show the difference in prototype activation vectors between the enhanced and original samples. The sharp increases in the plotted curves indicate the timesteps at which the respective prototypes begin to emerge prominently.

**Trend analysis on a larger sample set.** To analyze the trend more comprehensively, we randomly select 100 sam-

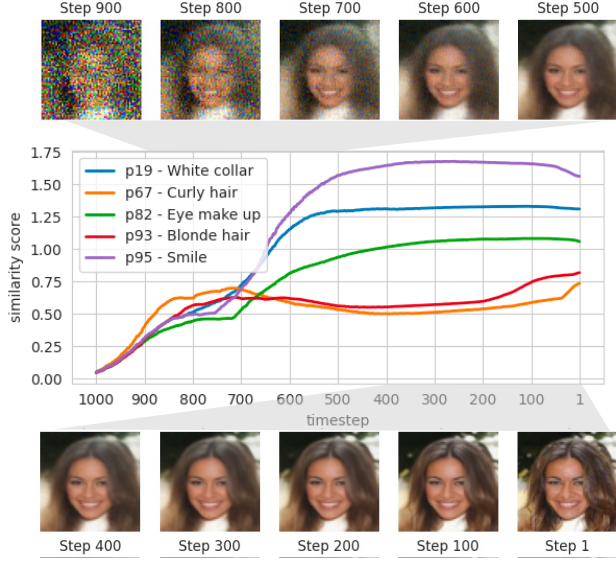


Figure 13. **Prototype emergence with added *White collar*.** Generation dynamics after introducing the *White collar* prototype.

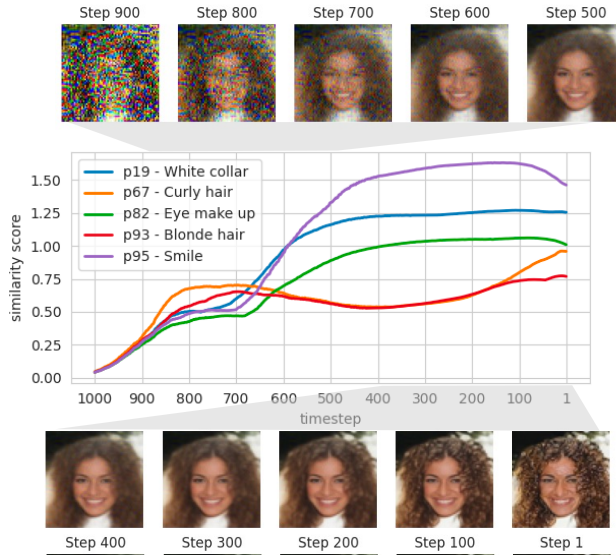


Figure 14. **Prototype emergence with added *Curly hair*.** Generation dynamics after introducing the *Curly hair* prototype.

ples from the test set and enhance all 100 prototypes for each sample. We then compute the average difference between the enhanced activation scores and their original values, visualizing the results as an averaged curve, just as shown in Fig. 9.

### A.3. Hyper-parameters for Training

More hyper-parameter for Patronus training could be found in Table 3. We trained all experiments with Adam optimizer, learning rate of  $1e^{-4}$ .

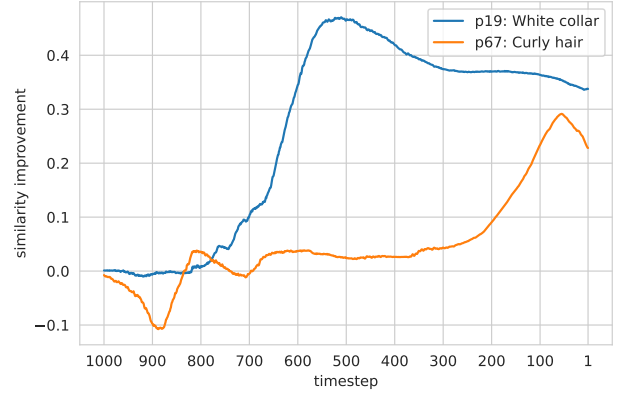


Figure 15. **Difference in prototype activations over time.** Sharp increases indicate timesteps when prototypes begin to emerge prominently in the enhanced sample compared to the original.

For the latent diffusion model, we trained with an 1D UNet, with base channels of 64, and channel multipliers as (1,2,4). We set the dropout rate as 0.2 and learning rate as  $1e^{-4}$ .

### A.4. CheXpert Dataset

In this work, we use a subset of the CheXpert dataset [12], retaining only frontal chest X-ray scans. To mitigate potential information leakage and reduce memorization effects due to patient-specific variations, we sample a single scan per patient<sup>2</sup>. This preprocessing step yields a total of 28,878 chest X-rays, of which 90% are allocated for training and the remaining 10% for testing.

## B. Ablation Study

As shown in Tab. 4, we present an ablation study of *Patronus* with respect to the number of prototypes and the dimensionality of the prototype vectors. Experiments are conducted on the CelebA dataset using an input resolution of (3, 64, 64), a training duration of 200 epochs, and a learning rate of  $1e^{-4}$ . Note that FID is computed in the context of conditional generation.

### B.1. Number of Prototypes

We evaluate the impact of varying the number of prototypes, setting  $\#p = \{32, 64, 100, 128\}$ , while fixing the prototype vector size to (1, 1, 128). As the number of prototypes increases, we observe consistent improvements in latent quality (measured by AUROC), the number of attributes captured, and the FID score. However, the TAD

<sup>2</sup>The number of recordings per patient in CheXpert is highly imbalanced, ranging from 1 to 89 [34]. Notably, disease severity is correlated with scan frequency—fewer than 25% of control subjects have more than five scans, while this proportion exceeds 50% among patients.



Table 3. Hyperparameters used for *Patronus* training.

	Input size	Num. p	shape of p	patch size	Num. patches	Num. Channels	Num. Channel. Mult
FashionMNIST	(1,32,32)	30	(1,1,128)	14×14	100	64	1,2,4,4
Cifar10	(3,32,32)	100	(1,1,128)	14×14	100	64	1,2,4,4
FFHQ	(3,64,64)	100	(1,1,128)	14×14	672	64	1,2,4,4
CelebA	(3,64,64)	100	(1,1,128)	14×14	672	64	1,2,4,4
CheXpert	(1,224,224)	100	(1,1,128)	60×60	1849	64	1,2,4,4

Table 4. Ablation study on CelebA, regarding the number of prototypes and the prototype vector size.

# p	shape of p	TAD ↑	Attrs ↑	Latent AUROC↑	FID ↓
32	(1,1,128)	$0.8291 \pm 0.0146$	$9.0000 \pm 0.0000$	$0.8288 \pm 0.0022$	$6.0126 \pm 0.0740$
64		<b><math>0.8515 \pm 0.0545</math></b>	$9.2000 \pm 0.4000$	$0.8527 \pm 0.0017$	$6.5395 \pm 0.0676$
100		$0.5395 \pm 0.1205$	$12.0000 \pm 1.0954$	$0.8646 \pm 0.0010$	$5.4871 \pm 0.0151$
128		$0.4700 \pm 0.0758$	<b><math>12.0000 \pm 0.8944</math></b>	<b><math>0.8713 \pm 0.0018</math></b>	<b><math>5.1264 \pm 0.0488</math></b>
64	(1,1,64)	$0.5860 \pm 0.0535$	$8.4000 \pm 0.4899$	$0.8491 \pm 0.0021$	$5.2017 \pm 0.0429$
	(1,1,128) *	<b><math>0.8515 \pm 0.0545</math></b>	$9.2000 \pm 0.4000$	$0.8527 \pm 0.0017$	$6.5395 \pm 0.0676$
	(1,1,256)	$0.4779 \pm 0.0045$	$8.0000 \pm 0.0000$	$0.8492 \pm 0.0008$	$6.2918 \pm 0.1279$

\* The result is the same as the second row since the hyper-parameters are identical. We listed it as another row for easier comparison.

score—which reflects the disentanglement quality—tends to decline. This trade-off is expected: while a larger prototype pool allows the model to capture more fine-grained visual patterns, it also introduces redundancy, reducing the distinctiveness and interpretability of individual prototypes. This suggests the existence of an optimal prototype budget for balancing generation quality and disentanglement.

## B.2. Prototype Vector Size

A larger prototype vector size allows each prototype to encode more detailed semantic information within a fixed spatial region. Conversely, when the prototype vector size is too small, the model may struggle to capture sufficient semantic richness. However, excessively large prototype vectors may introduce optimization challenges, such as slower convergence and increased redundancy. This trade-off is reflected in the results shown in Tab. 4, where a prototype vector size of (1, 1, 128) yields the best overall performance.

## C. Additional Results for Experiments

### C.1. Additional Visual Examples

**Reconstruction and Variation with Random  $x_T$**  We provide additional visual examples across multiple datasets in Fig. 16 (CelebA dataset) and Fig. 17 (FMNIST, Cifar10, and FFHQ datasets). These results demonstrate *Patronus*’ ability to capture semantic features across different datasets.

Notably, while *Patronus* effectively preserves fine details and patterns, it struggles with rare patterns. For instance, in the third row of Fig. 17a, the model fails to reconstruct the Adidas logo accurately. Another interesting case appears in the last row of Fig. 17c, where *Patronus* successfully identi-

Figure 16. Additional examples on reconstruction and variations with fixed  $s$  and random  $x_T$  with CelebA dataset.

fies the presence of a hat but generates variations of different hat styles instead of an exact reproduction.

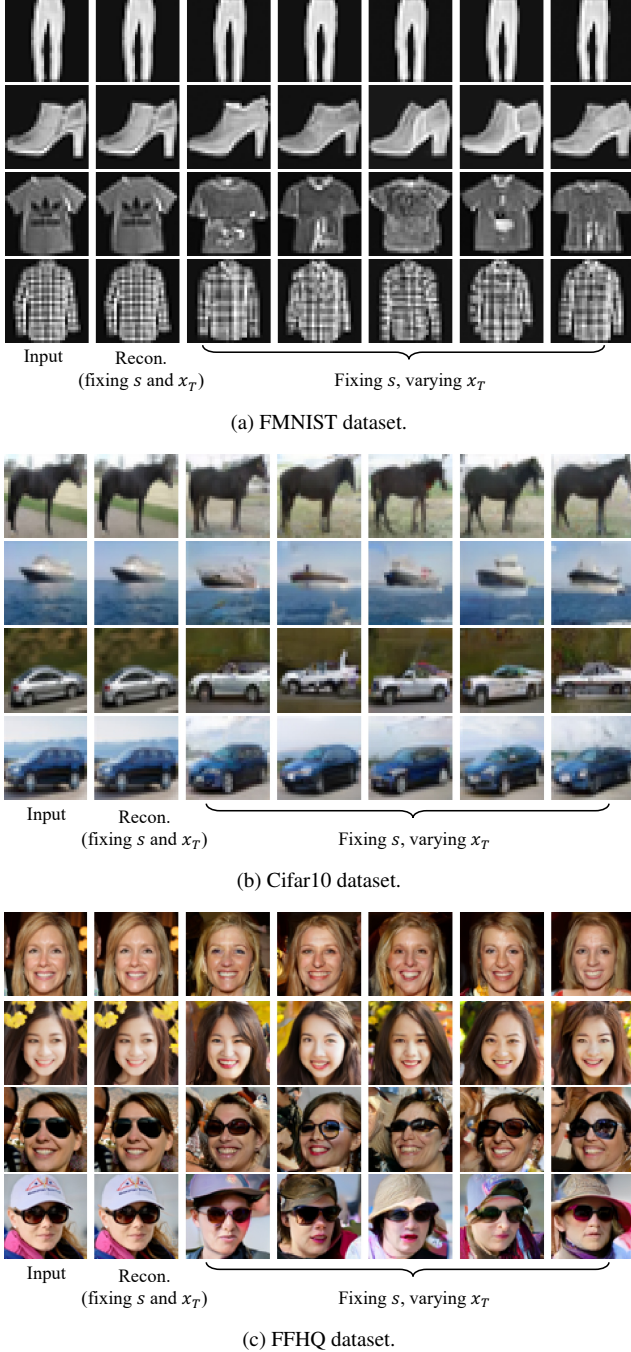


Figure 17. **Additional examples on reconstruction and variations with fixed  $s$  and random  $x_T$ :** FMNIST, Cifar10 and FFHQ.

**Interpolation** We provide additional visual examples of interpolation across various datasets, including CheXpert (Fig.18), as well as FMNIST, CIFAR-10, CelebA, and FFHQ (Fig.19). In datasets with well-defined class clusters, such as Fashion-MNIST and CIFAR-10, interpolation tends to be less effective when transitioning between images

belonging to different classes (Fig. 20).

### More Visual Samples for Diagnosis Ability of Patronus

In Fig.21, we present additional samples and hair-color-related prototypes for the diagnosis task, revealing a more pronounced bias—enhancing hair color also affects the presence of a smile. More specifically, we showcase eight cases, including four female and four male subjects. Within each gender group, we include two individuals with black hair and no smile, alongside one individual with brown or blonde hair and a smile. When enhancing black hair-related prototypes, all images transition to a non-smiling expression (as seen in the fourth and sixth columns of Fig.21).

## C.2. Visual Representation of Prototypes

We present a complete visual representation of the learned prototypes from the CelebA dataset in Fig. 22 and 23. Below each prototype, we provide a summary of its semantic meaning based on human observation without explicit annotation. Consequently, these interpretations may contain inaccuracies. For prototypes where a clear semantic meaning could not be determined, we leave the description blank. Notably, these blank descriptions highlight the inherent limitations of language in capturing visual concepts. The visualization process follows the steps outlined in Sec. 3.3.

## C.3. Captured Attributes by a Single Prototype

As shown in Tab. 1, we applied TAD and the number of attributes captured to estimate the prototype disentanglement ability, where *Patronus* remarkably outperformed the SOTA by nine captured attributes, whereas the previous methods only achieved at most three. We further explore which prototypes captured these attributes in Tab. 5, along with visualizations of the corresponding prototypes in Fig. 24.

As shown in Tab. 5, a single prototype can capture multiple attributes. E.g. prototype 82 captures both “Eyeglasses” and “Rosy\_Cheeks”. This finding is particularly interesting, as prior visual inspection suggested that prototype 82 represents the concept of “Heavy Eye Make-up” (Fig. 5), which is semantically related to both attributes: heavy eye make-up often co-occurs with rosy cheeks and tends to be negatively correlated with eyeglasses, possibly because individuals wearing heavy makeup are more likely to use contact lenses instead. This observation is further supported by the intervention results shown in Fig. 24, where suppressing the activation of  $p_{82}$  leads to the appearance of eyeglasses, while enhancing the activation induces both rosy cheeks and prominent eye make-up.

## C.4. Latent Quality for CheXpert Dataset

We analyze the latent quality for CheXpert dataset by measuring TAD, number of attributes being captured and latent AUROC in Tab. 6. A total of 23 attributes are eval-



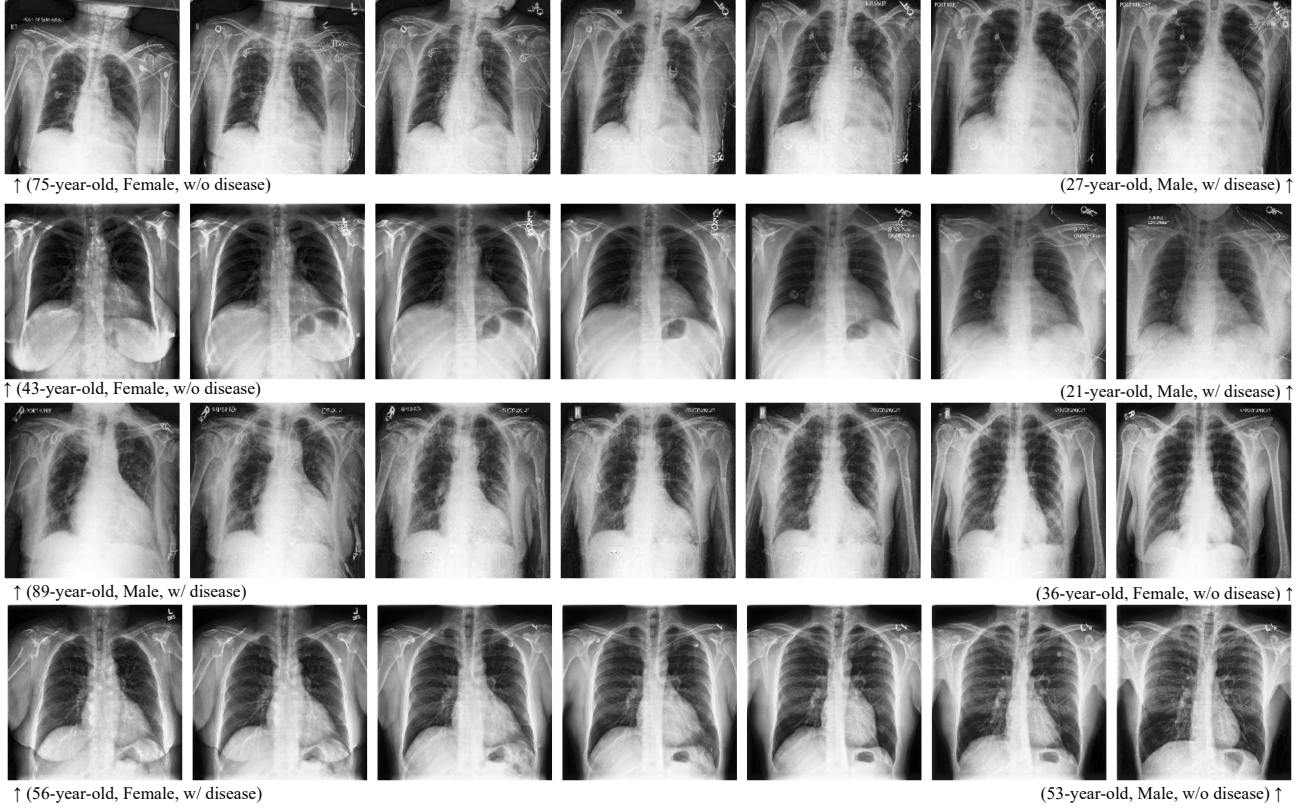


Figure 18. **Additional Examples of Image Interpolation on the CheXpert Dataset.** The interpolated sequences are generated between two real chest X-ray images. Each example displays the associated patient’s age, gender, and disease condition. The disease condition shown corresponds specifically to Cardiomegaly.

Table 5. **Captured Attributes in CelebA.**

Captured Attributes	Captured Attributes AUROC	Captured Prototype Index
Bald	$0.8276 \pm 0.0041$	30
Bangs	$0.8411 \pm 0.0022$	9
Black_Hair	$0.8104 \pm 0.0034$	78
Blond_Hair	$0.8917 \pm 0.0022$	93
Blurry	$0.8717 \pm 0.0058$	35
Eyeglasses	$0.7967 \pm 0.0026$	82
Pale_Skin	$0.8549 \pm 0.0044$	58
Rosy_Cheeks	$0.8226 \pm 0.0040$	82
Wearing_Hat	$0.9002 \pm 0.0025$	9

uated, comprising four demographic attributes, four indicators related to patients’ socioeconomic or health status, one shortcut feature pacemaker (annotated by [35]), and 14 disease-related labels. All attributes are binarized as detailed below<sup>3</sup>: Age ( $\geq 60$  or  $< 60$ ), Sex (Male or Female), Race (White or Non-white), Ethnicity (Hispanic/Latino or

<sup>3</sup>We acknowledge that the binarization is not ideal, as it may be white-centralized and introduce bias; however, it is adopted here for the sake of simplification.

Other), Insurance (Enrolled in Medicare or Not), Interpreter Need (Yes or No), Deceased (Yes or No), and BMI (within the normal range: 18.5–25.0, or outside).

**Evaluating latent quality.** As shown in Tab. 6, the learned latent representations demonstrate strong predictive capabilities for most demographic attributes, such as age, sex and BMI, achieving high AUROC scores using a simple logistic regression model. Notably, the latent space also encodes information relevant to the presence of a pacemaker. Furthermore, it supports the prediction of several cardiopulmonary conditions—such as Cardiomegaly, Edema, and Pleural Effusion—with AUROC values exceeding 0.75 (bold font in the table). These results indicate that the latent representations capture semantically meaningful and clinically relevant information. For comparison, we include the performance of a ResNet-50 baseline in the Tab. 6. It is worth noting that this baseline was trained on 320×320 resolution images [3], and that the original CheXpert validation set includes only samples from five disease categories. As a result, performance metrics for the remaining categories are unavailable.

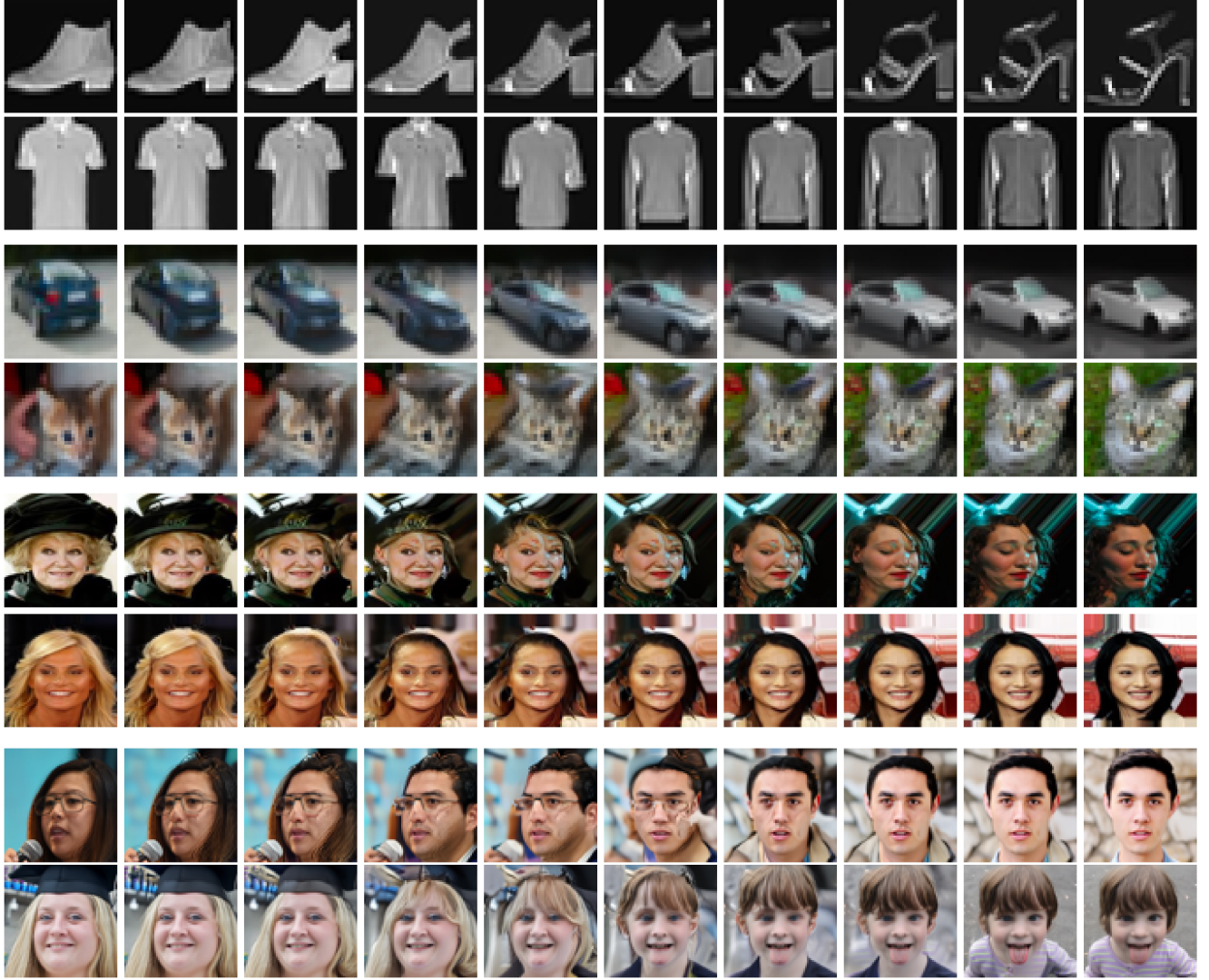


Figure 19. **Additional interpolation examples across multiple datasets.** Shown are interpolations between two images on Fashion-MNIST (first two rows), Cifar10 (third and fourth rows), CelebA (fifth and sixth rows), and FFHQ (seventh and eighth rows).



Figure 20. **Interpolation across classes in clustered datasets yields incoherent transitions.** For datasets with strong class-based clustering — such as Fashion-MNIST and Cifar10 — interpolation between samples from different classes often produces semantically implausible results, indicating that such interpolation may not be meaningful in these settings.



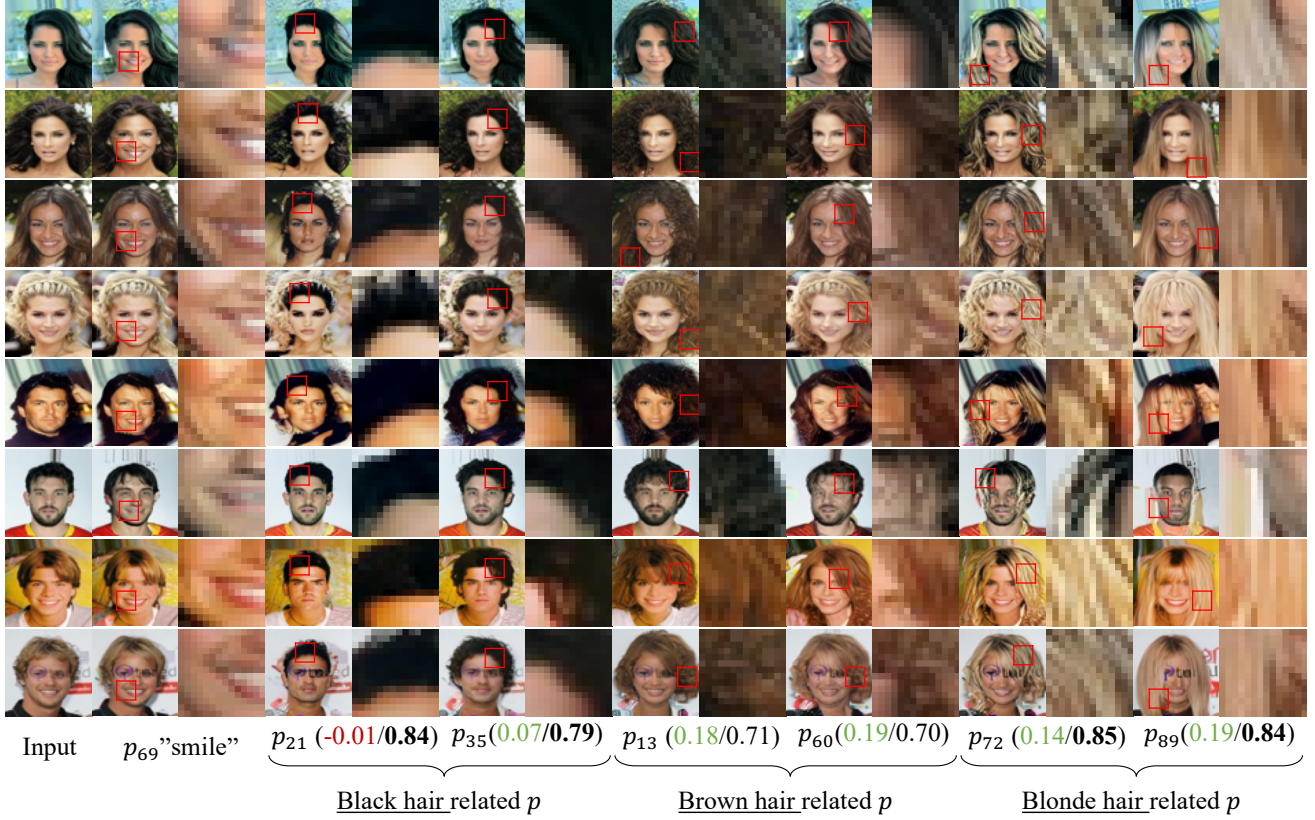


Figure 21. **More visual samples and more hair-color related prototypes for diagnosing unwanted correlations with *Patronus*.** By selecting the top two hair color prototypes (highest AUROC for single-dimension prediction), their correlation with “smile” prototype reveals dataset bias.  $p_j(a/b)$  define as: (a) Spearman correlation with the “smile” prototype (**green**: positive, **red**: negative), and (b) AUROC for predicting hair color when using this prototype (**bold** if  $\geq 0.75$ ).

Table 6. **Latent Quality of the CheXpert Dataset.** The *latent AUROC* denotes the average AUROC across all considered attributes. A total of 23 attributes are evaluated, comprising four demographic attributes, four indicators related to patients’ socioeconomic or health status, one shortcut feature (pacemaker), and 14 disease-related labels. All attributes are binarized. **Bolded** values indicate AUROC  $\geq 0.75$ .

TAD $\uparrow$	Attrs $\uparrow$	Latent AUROC $\uparrow$	Demographic Attributes*				Other Attributes*				Shortcut PM $\uparrow$	
			Age	Sex	Race	Ethnicity	Insurance	Interpreter	Deceased	BMI		
0.12 $\pm$ 0.01	3.0 $\pm$ 0.0	0.74 $\pm$ 0.01	<b>0.88<math>\pm</math>0.01</b>	<b>0.98<math>\pm</math>0.00</b>	0.70 $\pm$ 0.01	0.72 $\pm$ 0.01	0.74 $\pm$ 0.00	0.74 $\pm$ 0.00	0.66 $\pm$ 0.01	<b>0.77<math>\pm</math>0.01</b>	<b>0.92<math>\pm</math>0.01</b>	

	Disease Labels													
	No Finding	Enlarged CM $\ddagger$	Cardio-megaly	Lung Opacity	Lung Lesion	Edema	Consolidation	Pneumonia	Atelectasis	Pneumothorax	Pleural Effusion	Pleural Other	Fracture	Support Devices
LR using $p$	<b>0.86</b>	0.61	<b>0.75</b>	0.70	0.65	<b>0.77</b>	0.64	0.61	0.60	0.68	<b>0.80</b>	0.70	0.68	<b>0.76</b>
ResNet50 [3]	-	-	0.80	-	-	0.88	0.90	-	0.80	-	0.91	-	-	-

Captured Attributes	Captured Attributes AUROC	Captured Prototype Index
Age Group	0.7891 $\pm$ 0.0031	38
Sex	0.8806 $\pm$ 0.0005	1
PM $\uparrow$	0.7823 $\pm$ 0.0028	34

\* AUROC Performance from Latent Representations. The reported AUROC values reflect the performance of a logistic regression classifier trained on the latent representations using 5-fold cross-validation. Demographic and other attributes are binarized, details are in text.

$\uparrow$  Pacemaker, annotations from [35].

$\ddagger$  Enlarged Cardiomeastinum.

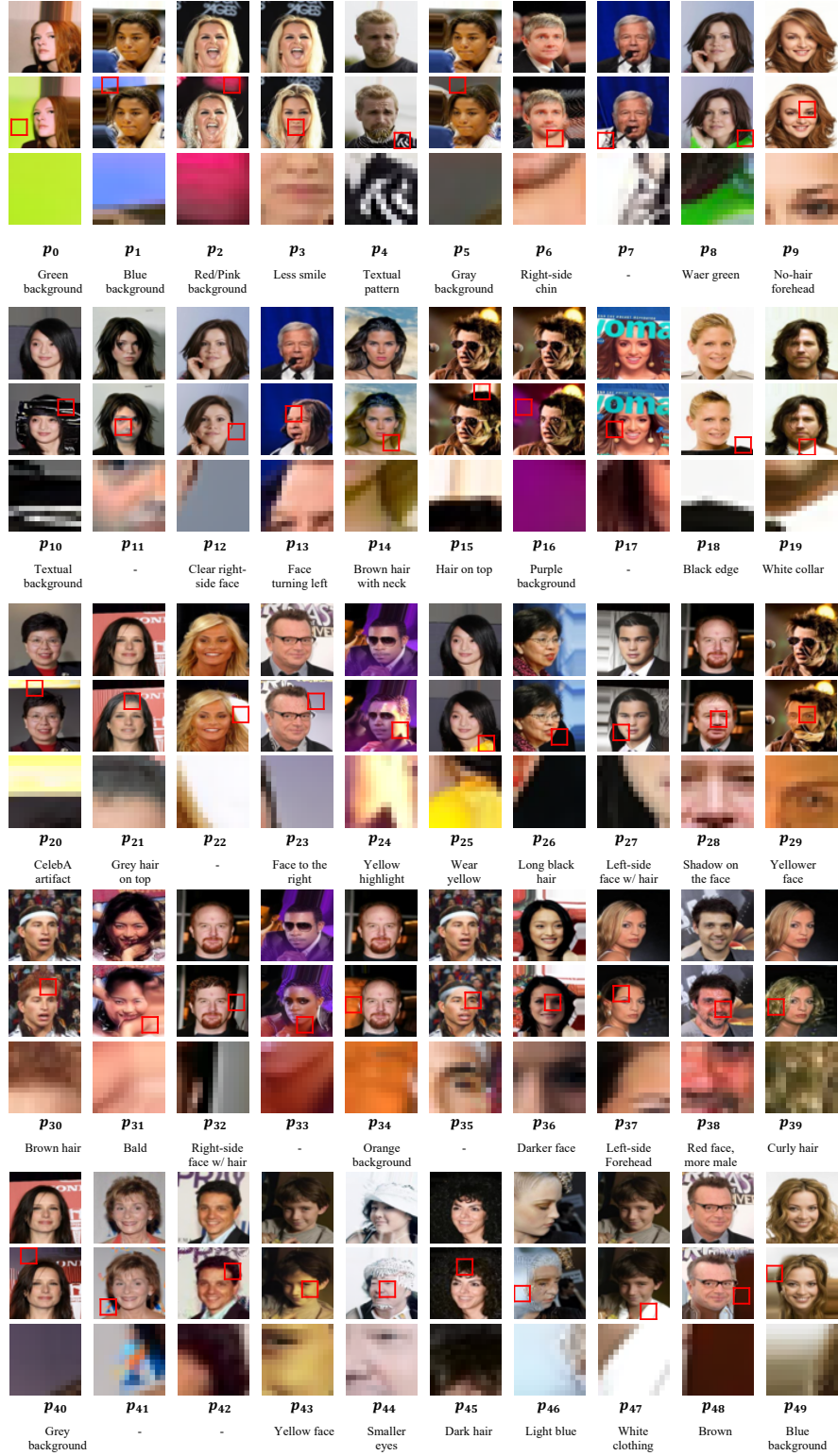


Figure 22. **Complete visualization of learned prototypes from the CelebA dataset (prototypes 0 to 49).** Each row contains 10 prototypes, with three types of data per prototype, displayed from top to bottom: the original image, the image enhanced with prototype  $j$ , and the most activated patch (serves as the prototype visualization).

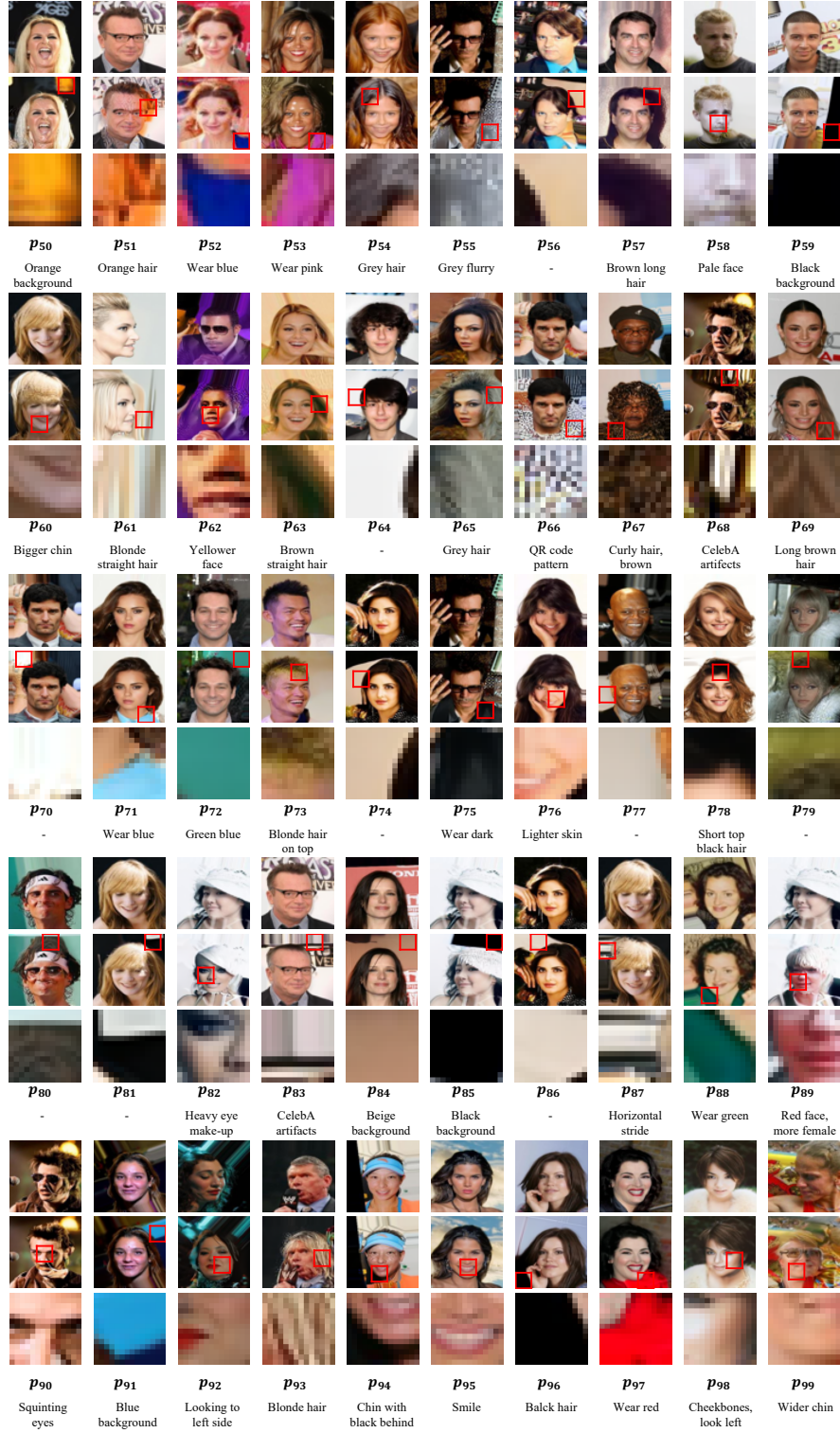


Figure 23. **Complete visualization of learned prototypes from the CelebA dataset (prototypes 50 to 99).** Each row contains 10 prototypes, with three types of data per prototype, displayed from top to bottom: the original image, the image enhanced with prototype  $j$ , and the most activated patch (serves as the prototype visualization).



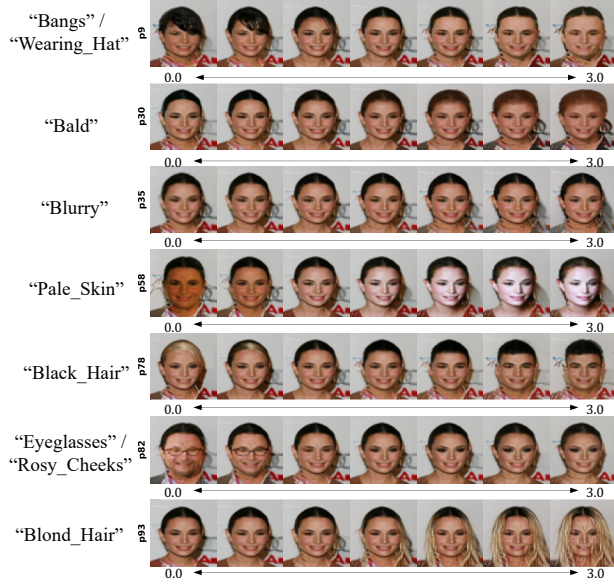
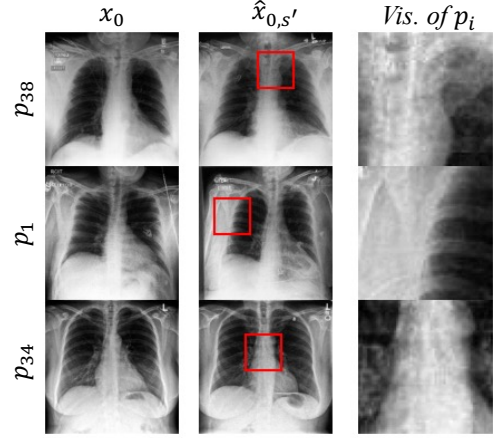


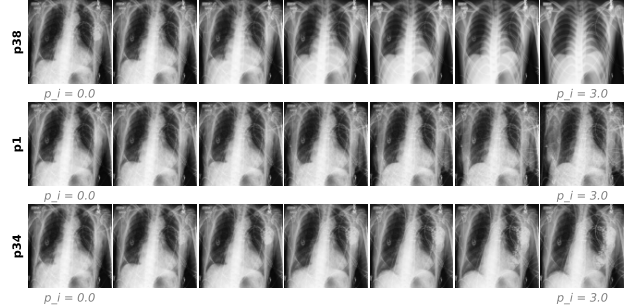
Figure 24. **Visualization of Captured Attributes in CelebA via Explorations.** The text on the left indicates the attributes captured in the CelebA dataset. Note that a single prototype can potentially capture multiple attributes.

**Interpreting Captured Attributes and Their Corresponding Prototypes.** Among the 23 attributes, three are captured by a single prototype, as listed in Tab. 6, with visualizations provided in Fig. 25. Notably, the **Sex** attribute is captured by a prototype that focuses on the edge of the chest wall (Fig. 25a). In the extrapolation experiment on prototype  $p_1$  (Fig. 25b), we observe a decrease in rib cage size as the prototype similarity score increases. This observation aligns with clinical findings that females tend to have a disproportionately smaller rib cage compared to males [1, 2]. For the **Age** attribute, the corresponding prototype is most activated in the region around the upper thoracic vertebrae (Fig. 25a). This may relate to the age-associated ossification of the costochondral cartilage of the first rib [23, 28]. Regarding the **Pacemaker** attribute, the most activated patch is located near the upper region of the heart, potentially reflecting the correlation between pacemaker presence and underlying cardiac conditions. In Fig. 25b, increasing the activation of prototype  $p_{34}$  leads to a more pronounced appearance of a pacemaker.

We acknowledge the limitations of our medical expertise and do not intend to draw definitive clinical conclusions from these observations. We welcome researchers with medical backgrounds to further evaluate and interpret these findings.



(a) Visualization of prototypes capturing attributes.



(b) Extrapolation over the same prototypes.

Figure 25. **Visualization and extrapolation of prototypes capturing attributes from CheXpert.** Three attributes are captured: Age (by  $p_{38}$ ), Sex (by  $p_1$ ), and presence of a pacemaker (by  $p_{34}$ ).

## D. Extended Discussion

**Do We Capture All Relevant Attributes?** We further illustrate the challenge of capturing global features with sample results in Fig. 26. Following the experiment described in Sec. 3, we reconstruct images and their variations using a fixed  $s$  with either fixed or random  $x_T$ . While fine-grained details, such as cheekbone structure in the second row and shirt details in the first row, are well preserved, the generated images with varying  $x_T$  fail to capture age or gender consistently on harder scenarios. For instance, the middle image in the first row appears noticeably younger than the original, while most variations in the second row depict a more mature appearance. Additionally, in the third sample, a gender shift from female to male is observed, possibly influenced by the presence of short hair.

**Justification for Excluding ProtoPNet’s Additional Loss Terms.** In this work, we optimize the model using only the denoiser loss. A key question arises: *Is this loss sufficient?* Except the attempt in adding extra loss for proto-



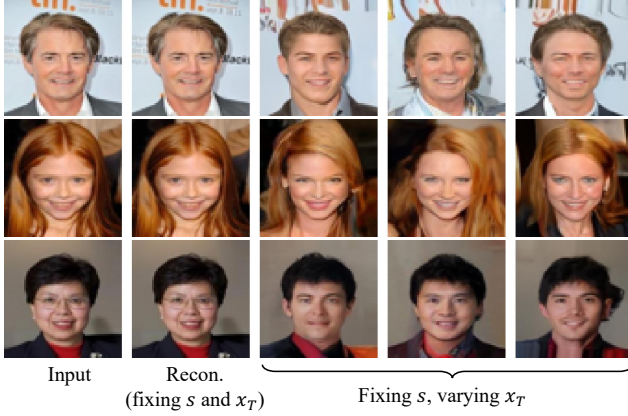


Figure 26. *Patronus* may struggle to capture global features such as age and gender. To illustrate this, we present three samples generated using the fixed  $s$  with random  $x_T$ . While the generated images successfully preserve semantic attributes such as hair color, cheekbones, smile, shirt, and background color, they fail to accurately reconstruct age or gender.

type disentanglement in Sec. 5 (Fig. 10), we further compare with ProtoPNet, which, alongside cross-entropy loss for classification, introduces two additional loss terms:

1. Cluster Loss (Clst): Ensures each training sample has at least one patch closely aligned with a learned prototype.
2. Separation Loss (Sep): Encourages each latent patch to remain distant from prototypes associated with different classes.

Neither loss is applicable in our setting:

1. Our goal is to learn representative prototypes that capture the underlying data distribution, **not** to enforce proximity to specific training samples.
2. Since our method is generative and does not rely on class labels, class-dependent separation constraints are irrelevant.

Thus, the denoiser loss is sufficient in our setting, as the additional loss terms in ProtoPNet are not applicable to our objective.